

Bi-abundance ionization structure of the Wolf-Rayet planetary nebula PB 8

A. Danehkar^{1,2,3}

¹Department of Physics and Astronomy, Macquarie University, Sydney, NSW 2109, Australia

²Harvard-Smithsonian Center for Astrophysics, 60 Garden Street, Cambridge, MA 02138, USA

³Email: ashkbiz.danehkar@cfa.harvard.edu

(RECEIVED August 29, 2017; ACCEPTED January 3, 2018)

Abstract

The planetary nebula (PN) PB 8 around a [WN/WC]-hybrid central star is one of PNe with moderate abundance discrepancy factors (ADFs $\sim 2-3$), which could be an indication of a tiny fraction of metal-rich inclusions embedded in the nebula (bi-abundance). In this work, we have constructed photoionization models to reproduce the optical and infrared observations of the PN PB 8 using a non-LTE stellar model atmosphere ionizing source. A chemically homogeneous model initially used cannot predict the optical recombination lines (ORLs). However, a bi-abundance model provides a better fit to most of the observed ORLs from N and O ions. The metal-rich inclusions in the bi-abundance model occupy 5.6 percent of the total volume of the nebula, and are roughly 1.7 times cooler and denser than the mean values of the surrounding nebula. The N/H and O/H abundance ratios in the metal-rich inclusions are ~ 1.0 and 1.7 dex larger than the diffuse warm nebula, respectively. To reproduce the *Spitzer* spectral energy distribution of PB 8, dust grains with a dust-to-gas ratio of 0.01 (by mass) were also included. It is found that the presence of metal-rich inclusions can explain the heavy element ORLs, while a dual-dust chemistry with different grain species and discrete grain sizes likely produces the infrared continuum of this PN. This study demonstrates that the bi-abundance hypothesis, which was examined in a few PNe with large abundance discrepancies (ADFs > 10), could also be applied to those typical PNe with moderate abundance discrepancies.

Keywords: ISM: abundances – planetary nebulae: individual (PB 8) – stars: Wolf-Rayet

1 INTRODUCTION

The planetary nebula (PN) PB 8 (PN G292.4+04.1) has been the subject of some recent studies (García-Rojas et al., 2009; Todt et al., 2010; Miller Bertolami et al., 2011). The central star of PB 8 has been classified as [WC 5-6] by Acker & Neiner (2003), as weak emission-line star type (*wels*; Tylenda et al., 1993; Gesicki et al., 2006), as [WC]-PG 1159 (Parthasarathy et al., 1998), and finally as [WN/WC] hybrid by Todt et al. (2010). Particularly, it is one of the rare stars, which has provoked a lot controversy about its evolutionary origin (Miller Bertolami et al., 2011). A detailed abundance analysis of the nebula by García-Rojas et al. (2009) showed abundance discrepancy factors (ADF \equiv ORL/CEL) of 2.57 for the O⁺⁺ ion and 1.94 for the N⁺⁺ ion, which are in the range of typical ADFs observed in PNe (ADFs $\sim 1.6-3.2$; see review

by Liu, 2006). The nebular morphology was described as a round nebula with inner knots or filaments by Stanghellini et al. (1993), and classified as elliptical by Gorny et al. (1997). However, a narrow-band H α + [N II] image of PB 8 taken by Schwarz et al. (1992) shows a roughly spherical nebula with an angular diameter of about 7 arcsec (6.5 arcsec \times 6.6 arcsec reported by Tylenda et al., 2003), which is used throughout this paper.

The ionic abundances of heavy elements derived from optical recombination lines (ORLs) have been found to be systematically higher than those derived from collisionally excited lines (CELs) in many PNe (see e.g. Rola & Stasińska, 1994; Liu et al., 2000, 2001, 2006; Tsamis et al., 2004, 2008; García-Rojas et al., 2009). To solve this problem, Liu et al. (2000) suggested a bi-abundance model in which the nebula contains two components of different abundances: cold hydrogen-deficient ‘metal-

Table 1 Journal of the Observations for PB 8.

Observatory	Obs Date	λ -range(\AA)	FWHM(\AA)	Inst./Mod.	Program ID/PI	Exp.Time (s)
Magellan 6.5-m	2006 May 9	3350–5050, 4950–9400	0.15, 0.25	MIKE	M. Peña	300, 600, 900
ANU 2.3-m	2010 Apr. 21	4415–5589, 5222–7070	0.83, 1.03	WiFeS	1100147, Q.A. Parker	60, 1200
<i>Spitzer</i>	2008 Feb. 25	5.2–14.5 μm , 14–38 μm	–	SL, LL	40115, G. Fazio	–

rich’ component and diffuse warm component of ‘normal’ abundances. The H-deficient inclusions embedded in the nebular gas of normal abundances can dominate the emissions of ORLs (Liu et al., 2000, 2004). The bi-abundance photoionization model of Abell 30 by Ercolano et al. (2003c) showed the possibility of such a scenario. More recently, the bi-abundance model by Yuan et al. (2011) was able to predict the ORLs in NGC 6153. Previously, the analysis of the emission-line spectrum of NGC 6153 by Liu et al. (2000) pointed to a component of the ionized gas, cold and very metal-rich. The photoionization modeling of NGC 1501 (Ercolano et al., 2004) and Abell 48 (Danehkar et al., 2014) also suggested that they may contain some cold H-deficient structures.

The aim of this paper is to construct photoionization models of PB 8, for which high quality spectroscopy has become available (García-Rojas et al., 2009), constrained by an ionizing source determined using the Potsdam Wolf-Rayet (PoWR) models for expanding atmospheres (Todt et al., 2010). To reproduce the observed ORLs, a bi-abundance model is used, which consists of a chemically homogeneous abundance distribution containing a small fraction of dense metal-rich structures. In addition, the dust properties are constrained using the *Spitzer* infrared (IR) continuum of the PN PB 8. The observations and modeling procedure are respectively described in Sections 2 and 3. In Section 4, we present our modeling results, while our conclusions are given in Section 5.

2 OBSERVATIONS

Deep optical long-slit spectra of the PN PB 8 were obtained at Las Campanas Observatory (PI: M. Peña), using the 6.5-m Magellan telescope and the double echelle Magellan Inamori Kyocera Echelle (MIKE) spectrograph on 9 May 2006 (García-Rojas et al., 2009). An observational journal is presented in Table 1. The standard grating settings used yield wavelength coverage from 3350–5050 \AA in the blue and 4950–9400 \AA in the red. The mean spectral resolution is 0.15 \AA FWHM in the blue and 0.25 \AA FWHM in the red. The MIKE observations were taken with three individual exposures of 300, 600 and 900 sec using a slit of 1×5 arcsec² and a position angle (PA) of 345° passing through the central star. To prevent contamination of the stellar continuum,

Table 2 IR line fluxes of the PN PB 8.

Lines	$F(\lambda)$ 10 ⁻¹² erg cm ⁻² s ⁻¹	$I(\lambda)$ [$I(\text{H}\beta) = 100$]
[Ar III] 8.99 μm	2.95	14.97
[Ne II] 12.82 μm	4.80	24.37
[Ne III] 15.55 μm	21.60	110.66
[S III] 18.68 μm	10.80	54.82
[S III] 33.65 μm	5.98	30.36
[Ne III] 36.02 μm	1.45	7.36

Note. Fig. 5 shows the *Spitzer* spectrum (SL & LL combined).

an area of 0.9×1 arcsec² on a bright knot located in the northern part of the slit was used to extract the nebular spectrum. However, there is no definite constraint on the location of the combined slit spectrum for the bright knot in the nebula, as the slit crossed over the nebula during the three different observations.¹ The top and bottom panels of Figure 1 show the blue and red spectra of PB 8 extracted from the 2D MIKE echellograms, normalized such that $F(\text{H}\beta) = 100$. As seen, several recombination lines from heavy element ions have been observed.

Infrared (IR) spectra of the PN PB 8 were taken on 25 February 2008 with the IR spectrograph on board the *Spitzer* Space Telescope (programme ID 40115, PI: Giovanni Fazio). The flux calibrated IR spectra used in this paper have been obtained from the Cornell Atlas of *Spitzer* / Infrared Spectrograph Sources² (CASSIS; Lebouteiller et al., 2011, 2015). The *Spitzer* observations were taken with two low-resolution modules: Short-Low (SL) and Long-Low (LL). The SL spectrum was taken with an aperture size of 3.7×57 arcsec² covering a wavelength coverage of 5.2–14.5 μm , whereas the LL spectrum has a wavelength coverage of 14.0–38.0 μm and an aperture size of 10.7×168 arcsec². As the LL aperture is larger than the SL aperture, the LL module collects more flux than the SL, including the surrounding background contamination. This causes a jump at around 14 μm between the SL and the LL. To correct it,

¹The MIKE spectrograph was not attached to any telescope rotator in 2006, so the slit passes over the nebula in each observation (García-Rojas, private communications, 2014).

²The Cornell Atlas of *Spitzer*/IRS Sources (CASSIS) is a product of the Infrared Science Center at Cornell University, supported by NASA and JPL. Website: <http://cassis.astro.cornell.edu>

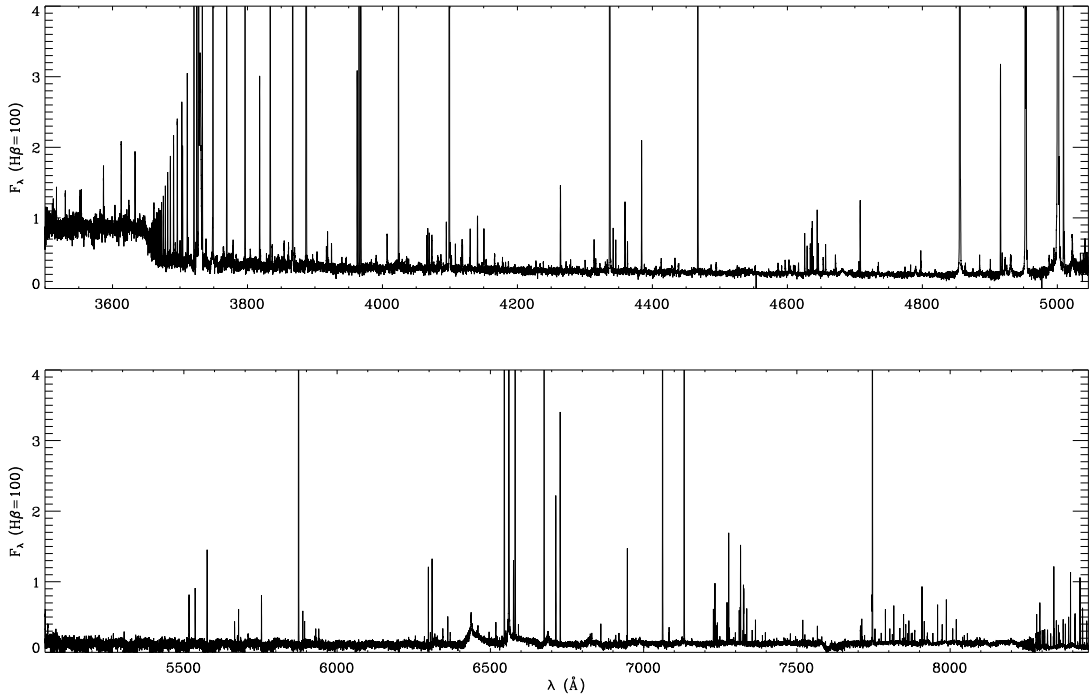


Figure 1. The observed optical spectrum of the PN PB 8 (García-Rojas et al., 2009), covering wavelengths of (top) 3500–5046 Å and (bottom) 5047–8451 Å, and normalized such that $F(\text{H}\beta) = 100$.

the LL spectrum was scaled to match the SL spectrum, so the combined *Spitzer* spectrum describes the thermal IR emission of the nebula with little background contribution. Table 2 lists the line fluxes measured from the *Spitzer* IR spectra (see Fig. 5 for the *Spitzer* SL and LL combined spectrum). The intrinsic line fluxes presented in column 3 are on a scale where $I(\text{H}\beta) = 100$, and the dereddened flux $I(\text{H}\beta) = 19.7 \times 10^{-12} \text{ erg cm}^{-2} \text{ s}^{-1}$ calculated using the total $\text{H}\alpha$ flux (Frew et al., 2013), $E(B - V) = 0.41$ and $R_V = 4$ (Todt et al., 2010).

Integral field unit (IFU) spectra were obtained at the Siding Spring Observatory on 21 April 2010 (programme ID 1100147, PI: Q.A. Parker), using the 2.3-m ANU telescope and the Wide Field Spectrograph (WiFeS; Dopita et al., 2007, 2010). The settings used were the B7000/R7000 grating combination and the RT 560 dichroic, giving wavelength coverage from 4415–5589 Å in the blue and 5222–7070 Å in the red, and mean spectral resolution of 0.83 Å FWHM in the blue and 1.03 Å FWHM in the red (see the observational journal presented in Table 1). The WiFeS IFU rawdata were reduced using the IRAF pipeline *wifes*, which consists of bias-reduction, sky-subtraction, flat-fielding, wavelength calibration using Cu-Ar arc exposures, spatial calibration using wire frames, differential atmospheric refraction correction, and flux calibration using spectrophotometric standard stars EG 274 and LTT 3864 (fully described in Danehkar et al., 2013, 2014).

Figure 2 shows the spatially resolved flux intensity and radial velocity maps of PB8 extracted from the emission line $[\text{N II}] \lambda 6584$ for spaxels across the WiFeS IFU field. The black/white contour lines depict the distribution of the emission of $\text{H}\alpha$ obtained from the SuperCOSMOS $\text{H}\alpha$ Sky Survey (SHS; Parker et al., 2005), which can aid us in distinguishing the nebular borders. The emission line maps were obtained from solutions of the nonlinear least-squares minimization to a Gaussian curve function for each spaxel. The observed velocity V_{obs} was transferred to the local standard of rest (LSR) radial velocity V_{LSR} . The WiFeS IFU observations have recently been used for morpho-kinematic studies of PNe (Danahkar, 2015; Danahkar et al., 2016). Considering the spatial resolution of the WiFeS (1 arcsec), this PN is very compact for detailed morpho-kinematic modeling. Following Danahkar & Parker (2015), the tenuous lobes of PB 8 extending from its compact core can be used to determine its spatial orientation. As seen in Figure 2, the orientation of its faint lobes onto the plane of the sky has a position angle of $132^\circ \pm 8^\circ$ relative to the north equatorial pole towards the east. Transferring into the Galactic coordinate system, its symmetric axis has a Galactic position angle of $114.6^\circ \pm 8^\circ$, measured from the north Galactic pole towards the Galactic east, approximately aligned with the Galactic plane.

We obtained an expansion velocity of $V_{\text{exp}} = 20 \pm 4 \text{ km s}^{-1}$ from the $[\text{N II}] \lambda 6584$ flux integrated across the

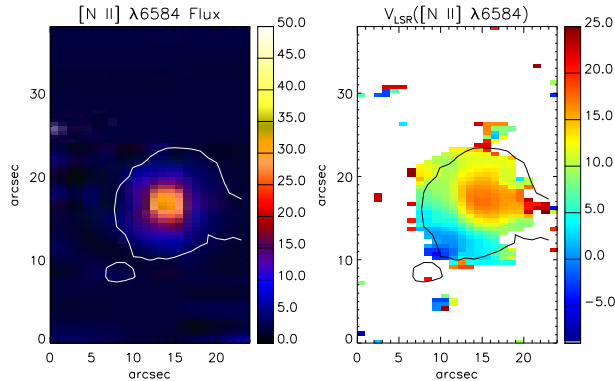


Figure 2. Maps of PB 8 in [N II] $\lambda 6584$ from the IFU observation. From left to right: spatial distribution maps of flux intensity and LSR velocity. Flux unit is in $10^{-15} \text{ erg s}^{-1} \text{ cm}^{-2} \text{ spaxel}^{-1}$, and velocity in km s^{-1} . North is up and east is toward the left-hand side. The white/black contour lines show the distribution of the narrow-band emission of H α in arbitrary unit obtained from the SHS (Parker et al., 2005).

whole nebula in the WiFeS field, which is in agreement with $V_{\text{exp}} = 19 \text{ km s}^{-1}$ from [N II] $\lambda 6584$ line derived by Todt et al. (2010). Moreover, García-Rojas et al. (2009) derived an expansion velocity of $V_{\text{exp}} = 14 \pm 2 \text{ km s}^{-1}$ from the [O III] $\lambda 5007$ line, which is associated with a different ionization zone. García-Rojas et al. (2009) obtained $V_{\text{sys}} = 1.4 \text{ km s}^{-1}$ from [O III] lines, in agreement with the value of $V_{\text{sys}} = 2.4 \text{ km s}^{-1}$ given by Todt et al. (2010).

3 PHOTOIONIZATION MODELING

The photoionization modeling is performed using the MOCASSIN code (version 2.02.70), described in detail by Ercolano et al. (2003a, 2005) in which the radiative transfer of the stellar and diffuse field is computed using a Monte Carlo (MC) method constructed in a cubical Cartesian grid, allowing completely arbitrary distribution of nebular density and chemical abundances. This code has already been used to study some chemical inhomogeneous models, namely the H-deficient knots of Abell 30 (Ercolano et al., 2003c) and the super-metal-rich knots of NGC 6153 (Yuan et al., 2011). To solve the problem of ORL-CEL abundance discrepancies in those PNe, they used a metal-rich component, whose ratios of heavy elements with respect to H are higher than those of the normal component.

To investigate the abundance discrepancies between the ORLs and CELs, we have constructed different photoionization models for PB 8. We run a set of model simulations, from which we finally selected three models, which best reproduced the observations. Our first model (MC1) consists of a chemically homogeneous abundance distribution. Our second model (MC2) is roughly similar, but it includes some dense metal-rich knots (cells)

embedded in the density model of normal abundances (see Section 3.2). The final model (MC3) includes dust grains to match the *Spitzer* IR observation (see Section 3.4). The atomic data sets used for our models include energy levels, collision strengths, and transition probabilities from Version 7.0 of the CHIANTI database (Landi et al., 2012, and references therein), hydrogen and helium free-bound coefficients of Ercolano & Storey (2006), and opacities from Verner et al. (1993) and Verner & Yakovlev (1995).

The model parameters, as well as the physical properties for the models, are summarized in Table 3, and discussed in more detail in the following sections. The modeling procedure consists of an iterative process, involving the comparison of the predicted emission line fluxes with the values measured from the observations, and the ionization and thermal structures with the values derived from the empirical analysis. The free parameters used in our models should be the nebular abundances, as the nebular density is adopted based on empirical results (García-Rojas et al., 2009), and the stellar parameters based on the model atmosphere study (Todt et al., 2010). However, it is impossible to isolate effects of any parameter from each other, as they are dependent on each other, so we cannot just modify the nebular abundances without slightly adjusting the density distribution and the distance. The nebular ionization structure depends on the gas density and the stellar characteristics, so we fairly adjusted them to obtain the best-fitting models. We adopted the effective temperature of $T_{\text{eff}} = 52 \text{ kK}$, stellar luminosity of $L_{\star} = 6000 L_{\odot}$, and non-local thermodynamic equilibrium (non-LTE) model atmosphere determined by Todt et al. (2010). The optical depth for Lyman-continuum radiation of $\tau(\text{Ly-c}) = 0.63$ estimated by Lenzuni et al. (1989) indicated some ionizing radiation fields may escape from the nebular shell, so it could be a matter-bounded PN. Therefore, we attempted to adjust distance and gas density to reproduce the nebular total H β intrinsic line flux. It is found that a model with an electron density of about $2550 \pm 550 \text{ cm}^{-3}$ empirically derived by García-Rojas et al. (2009) can well reproduce the nebular H β intrinsic line flux at a distance of 4.9 kpc. We initially used the elemental abundances determined by García-Rojas et al. (2009), but we adjusted them to match the observed nebular spectrum.

3.1 The ionizing spectrum

The H-deficient non-LTE model atmosphere (Todt et al., 2010), which was calculated using the PoWR models for expanding atmospheres (Gräfener et al., 2002; Hamann & Gräfener, 2004), was used as an ionizing source in our photoionization models. The PoWR models were constructed by solving the non-LTE radiative transfer equation of an expanding stellar at-

Table 3 Model parameters and physical properties for the final photoionization models.

Parameter	Empirical		Models						
	CEL	ORL	MC1	Normal	MC2 Metal-rich	Total	Normal	MC3 Metal-rich	Total
T_{eff} (kK)	52		52		52			52	
L_{\star} (L_{\odot})	6000		6000		6000			6000	
R_{in} (10^{17} cm)	–		0.8		0.8			0.8	
R_{out} (10^{17} cm)	–		2.6		2.6			2.6	
Filling factor	–		1.000	0.944	0.056	1.000	0.944	0.056	1.000
$\langle N(\text{H}^+) \rangle$ (cm^{-3})	–		2009	1957	3300	2032	1957	3300	2032
$\langle N_{\text{e}} \rangle$ (cm^{-3})	2550 \pm 550		2257	2199	4012	2301	2199	4012	2301
$\rho_{\text{d}}/\rho_{\text{g}}$	–		–		–			–	0.01
He/H	–	0.122	0.122	0.122	0.20	0.129	0.122	0.20	0.129
C/H $\times 10^5$	–	72.25	63.0	63.0	63.0	63.0	63.0	63.0	63.0
N/H $\times 10^5$	16.22	31.41 ^a	11.0	6.1	298.0 ^a	32.7 ^a	6.1	298.0 ^a	32.7 ^a
O/H $\times 10^5$	57.54	146.61 ^a	40.0	58.7	551.0 ^a	103.5 ^a	58.7	551.0 ^a	103.5 ^a
Ne/H $\times 10^5$	13.49	19.9 ^a	10.0	15.0	15.0 ^a	15.0 ^a	15.0	15.0 ^a	15.0 ^a
S/H $\times 10^7$	204.17	–	300.0	300.0	300.0	300.0	300.0	300.0	300.0
Cl/H $\times 10^7$	2.0	–	1.2	1.6	1.6	1.6	1.6	1.6	1.6
Ar/H $\times 10^7$	43.65	–	39.0	45.0	45.0	45.0	45.0	45.0	45.0

^a The ORL empirical abundances were calculated from the ORLs over the total H^+ emission flux, emitted from both the diffuse gas and metal-rich inclusion, so the empirical abundances of the ORLs cannot be the same as the model metal-rich component, but roughly similar to the mean total abundances of both the metal-rich and normal components.

mosphere under the assumptions of spherical symmetry and chemical homogeneity. The PoWR model used was calculated for the stellar surface abundances $\text{H}:\text{He}:\text{C}:\text{N}:\text{O} = 40:55:1.3:2:1.3$ (by mass), the stellar temperature $T_{\text{eff}} = 52$ kK, the stellar luminosity $L_{\star} = 6000L_{\odot}$, the transformed radius $\log R_{\text{t}} = 1.43R_{\odot}$ and the wind terminal velocity $V_{\infty} = 1000 \text{ km s}^{-1}$, which well matches the dereddened stellar spectra from FUSE, IUE and MIKE, as well as 2MASS JHK bands (Todt et al., 2010). We see that the nebular $[\text{O III}] \lambda 5007$ line flux relative to the $\text{H}\beta$ flux is well reproduced with an effective temperature of $T_{\text{eff}} = 52$ kK in our photoionization models. The stellar luminosity of $L_{\star} = 6000L_{\odot}$ adopted by Todt et al. (2010) is related to a remnant core with a typical mass of $0.6M_{\odot}$ (e.g. Miller Bertolami & Althaus, 2007; Schönberner et al., 005a). The distance was also varied in order to reproduce the nebular emission-line fluxes, under the constraints of our adopted stellar parameters and spherical density distribution. The best results for the photoionization models were obtained at a distance of 4.9 kpc.

Figure 3 compares the non-LTE model atmosphere flux of PB 8 with a blackbody flux at the same temperature. At energies higher than 54 eV (He II ground state), there is a significant difference between the non-LTE model atmosphere and blackbody flux. As discussed by Rauch (2003), a blackbody is not an accurate representation of the ionizing flux. The H-deficient non-LTE model atmosphere has a major departure from the solar model atmosphere at higher energies due to the small opacity from hydrogen. In our photoionization models, we theretofore used an non-LTE model atmosphere as

the ionizing source to provide the best fit to the nebular spectrum. However, the difference may not be largely noticeable in our model as high-excitation lines (e.g. He II) are not observed.

3.2 The density distribution

The initial nebular model to be run was the simplest possible density distribution, a homogeneous spherical geometry, to reproduce the CELs. The chemical abundances were taken to be homogeneous. A first attempt was made by using a homogeneous density distribution of 2550 cm^{-3} with different inner and outer radii, deduced from the $[\text{O II}]$, $[\text{S II}]$ and $[\text{Cl III}]$ lines (García-Rojas et al., 2009). However, the uniform density distribution did not match the ionization and thermal structures, so we examined different density distributions adopted based on radiation-hydrodynamics simulations (see e.g. Perinotto et al., 2004; Schönberner et al., 005a,b) to make the best fit to the observed CELs, and also to constrain the shell thickness. Some radiation-hydrodynamics results depict a radial density profile having the form $N_{\text{H}}(r) = N_0[(r_{\text{out}}/r)^{\alpha}]$, where r is the radial distance from the center, α the radial density dependence, N_0 the characteristic density, r_{out} the outer radius. We finally adopted a density distribution with a powerlaw radial profile. Figure 4 illustrates the 3-D spherical density model constructed based on the radial density profile, and the ionizing source is located in the corner. We chose the characteristic density of $N_0 = 2600 \text{ cm}^{-3}$ and the radial density dependence of $\alpha = -1$. The outer radius of the sphere is equal to

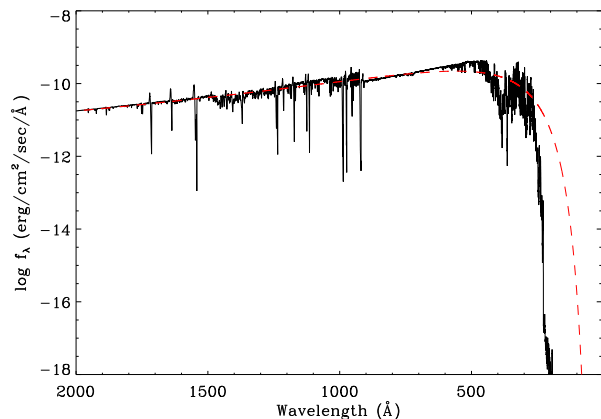


Figure 3. Non-LTE model atmosphere (solid line) calculated with $T_{\text{eff}} = 52$ kK and chemical abundance ratio of H:He:C:N:O = 40:55:1.3:2:1.3 by mass (Todt et al., 2010), compared with a blackbody (dashed line) at the same temperature.

Table 4 Metal-rich component parameters in the model MC2.

Parameter	Value
Filling factor	0.056
Mass fraction	6.3 percent
Number of knots	33
Knot size (arcsec ³)	(0.35) ³
$\langle N(\text{H}^+) \rangle$ (cm ⁻³)	3300
$\langle N_e \rangle$ (cm ⁻³)	4012
$\langle T_e \rangle$ (K)	4286

$R_{\text{out}} = 3.5$ arcsec and the thickness is $\delta R = 2.4$ arcsec. We examined distances, with values within the range of distances 2.2 and 5.8 kpc (Phillips, 2004, and references therein). The distance of $D = 4.9$ kpc found here, was chosen, because of the best predicted $\text{H}\beta$ luminosity $L(\text{H}\beta) = 4\pi D^2 I(\text{H}\beta)$, and it is within the range of distances 4.2 and 5.15 kpc estimated by Todt et al. (2010). Taking the angular diameter of 7 arcsec, we derive an outer radius of $R_{\text{out}} = 2.6 \times 10^{17}$ cm at the given distance of $D = 4.9$ kpc.

A second attempt (MC2) was to reproduce the observed ORLs by introducing a fraction of metal-rich knots into the density distribution used by the first model. The abundance ratios of He, N, and O relative to H in the metal-rich component are higher than those in the normal component. Two different bi-abundance models suggested by Liu et al. (2000): one assumes that H-deficient component with a very high density ($N_e = 2 \times 10^6$ cm⁻³) and a moderate temperature ($T_e = 4700$ K), which has been adopted in the bi-abundance photoionization model of Abell 30 (Ercolano et al., 2003c) and NGC 6153 (Yuan et al., 2011). However, H-deficient component in the second model intro-

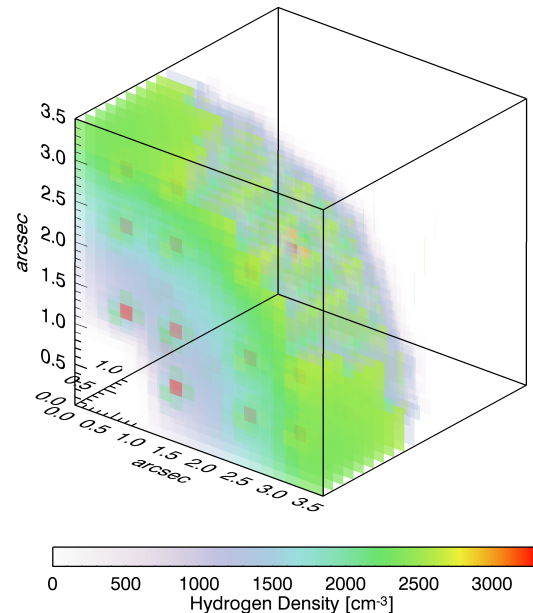


Figure 4. Spherical density distribution a powerlaw radial profile adopted for photoionization models. The sphere has outer radius of 3.5 arcsec and thickness of 2.4 arcsec. The ionizing source is placed in the corner (0, 0, 0). Metal-rich inclusions are shown as a darker knots with $N_H = 3300$ cm⁻³ embedded in the density model of normal abundances. The units of the axes are arcsec.

duced by Liu et al. (2000) has an 8 times lower N_e and a 20 times lower T_e than the normal component. After exploring both the assumptions, we adopted a dense metal-rich component with the H number density of 3300 cm⁻³, which is roughly 1.7 times higher than the mean density of the surrounding material.

In Figure 4, the 3-D spatial distribution of metal-rich knots (cells) are shown as a darker shade inside the density model of normal abundances. The gas-filling factor in the density model MC1 was kept at unity, while the inclusion of 33 metal-rich cells in the normal abundances nebula in the model MC2 (see Table 4) leads to gas-filling factors of 0.056 for the metal-rich component. It means that the dense metal-rich inclusions occupy 5.6 percent of the total gaseous volume of the nebula. Higher values of the gas-filling factor for the metal-rich component require lower values of the number density in order to reproduce the ORLs, but they may not provide the best match. We note that the filling factor parameter in MOCASSIN is still set to 1.0, which can have a major role in emission-line calculations. For example, reducing the MOCASSIN filling factor parameter from 1.0 to 0.5 decreases the nebular $\text{H}\beta$ luminosity by a factor of 2 and increases the $[\text{O III}] \lambda 5007/\text{H}\beta$ flux ratio by 9 percent, so the nebula cannot be reproduced.

For our bi-abundance model, we assume 33 metal-rich knots are uniformly distributed inside the diffuse warm nebula. However, Ercolano et al. (2003c) adopted

a dense core surrounded by a less dense outer region in the bi-abundance model of Abell 30. Moreover, the metal-rich inclusions were distributed in the inner region of the diffuse warm nebula in the bi-abundance model of NGC 6153 (Yuan et al., 2011). Adopting the current knot density (3300 cm^{-3}) in PB 8, different distributions of metal-rich knots require totally different N/H and O/H abundance ratios and filling factors, which may not be in pressure equilibrium with their diffuse warm nebula. We note that ADFs of Abell 30 and NGC 6153 are very large, and are not similar to moderate ADFs of PB 8. Moreover, the effective temperatures of the central stars of Abell 30 and NGC 6153 are 130 000 and 90 000 K, respectively, which are hotter than $T_{\text{eff}} = 52 000 \text{ K}$ in PB 8. This indicates that the central star of PB 8 is in an early stage of its evolutionary path towards becoming a white dwarf, and should be younger than the hot central stars of Abell 30 and NGC 6153.

The physical size of the metal-rich knots also play an important role in making an ionization structure to reproduce the N II and O II ORLs. It is found that the physical size of $(0.008)^3 \text{ parsec}^3$ (at $D = 4.9 \text{ kpc}$) can well produce the observed ORLs. Reducing the physical size will lead to an increase in the number of knots, which also need different density or/and N/H and O/H abundance ratios to match the observation. Smaller sizes will contribute to higher ionization and more thermal effects (see also Yuan et al., 2011), so we may not be able to reproduce electron temperatures estimated from the ORLs (see Section 4.2). A larger physical size will also decrease the number of knots, but it needs different density or/and different elemental abundances of N and O, which may not make metal-rich inclusions in pressure equilibrium with the surrounding gas.

3.3 The nebular elemental abundances

We used a homogeneous chemical abundance distribution for the model MC1 consisting of 9 elements, including all the major contributors to the thermal balance of the nebula and those producing the density- and temperature-sensitive CELs. The abundances derived from the empirical analysis (García-Rojas et al., 2009) were chosen as starting values; these were iteratively modified to get a better fit to the CELs. The final abundance values are listed in Table 3, where they are given by number with respect to H.

A two-component elemental abundance distribution was used for the model MC2 that yields a better fit to the observed ORLs. The parameters of the metal-rich cells included in the bi-abundance model MC2 are summarized in Table 4. The metal-rich inclusions were constructed using 33 knots with the physical size of $(0.35)^3 \text{ arcsec}^3$. As shown in Figure 4 (b), they are uniformly distributed inside the normal component model with

the same geometry, but a filling factor of 0.056. The initial guesses at the elemental abundances of N and O in the the metal-rich component were taken from the ORL empirical results; they were successively increased to fit the observed N II and O II ORLs. Table 3 lists the final elemental abundances (with respect to H) derived for both components, normal and metal-rich. The final model, which provided a better fit to most of the observed ORLs, has a total metal-rich mass of about 6.3 percent of the ionized mass of the entire nebula.

The O/H and N/H abundance ratios in the metal-rich component are about 1.0 and 1.7 dex larger than those in the normal component. The C/O abundance ratio in the metal-rich component less than unity is in disagreement with the theoretical predictions of born-again stellar models (Herwig, 2001; Althaus et al., 2005; Werner & Herwig, 2006). As seen in Table 3, the ORL total abundances empirically derived were not similar to the elemental abundances chosen for the model metal-rich component. This is due to the fact that the ORL empirical abundances were derived from the ORLs, emitted mainly from metal-rich inclusion, over the H^+ flux of the entire nebula, emitted from both the diffuse gas and metal-rich inclusion. Hence, the empirical abundances of the ORLs are roughly similar to the mean total abundances of both the metal-rich and normal components.

As seen in Table 3, the elemental abundance for neon does not show a large abundance discrepancy similar to what we see for oxygen and nitrogen, which is unlike to the bi-abundance models of Abell 30 (Ercolano et al., 2003c) and NGC 6153 (Yuan et al., 2011). We note that the H-deficient knots of Abell 30 shows ADF(Ne^{++}) values in the range of 400–1000 (Wesson et al., 2003), and NGC 6153 has a ADF(Ne^{++}) of about 60 (Liu et al., 2000). Nevertheless, PB 8 has ADF(Ne^{++}) = 1.48 (García-Rojas et al., 2009). To reproduce the spectrum of Abell 30, Ercolano et al. (2003c) also assumed a bi-abundance model, in which the metal-rich core has a density of about six times higher than the surrounding normal envelope. Thus, both Abell 30 and NGC 6153 have extremely large ADFs, which are dissimilar to PB 8. We should also include that the atomic data of the ORLs of Ne^{++} ion (Kisielius et al., 1998) used by MOCASSIN do not have any recombination coefficients for the Ne II $\lambda 4391.94$ and $\lambda 4409.30$ lines, while García-Rojas et al. (2009) employed different atomic data (Kisielius & Storey; unpublished) to derive Ne^{++} ion abundance from for Ne II ORLs.

It is worthwhile to mention that the AGB nucleosynthesis dramatically changes the composition of He, C and N (Karakas & Lattanzio, 2003; Karakas et al., 2009), but other elements such as Ne, S, Cl, and Ar are left untouched by the evolution and nucleosynthesis in low and intermediate-mass stars. In this typical PN with moderate ADFs, abundances of other elements heavier than oxygen such as neon in the metal-rich components

Table 5 Input parameters for the dust model of PB 8.

Grain Species	Weight	Ref. for optical constants
Amorphous Carbon	1	Hanner (1988)
Crystalline Silicate	1	Jaeger et al. (1994)
Grain Radius (μm)	Weight	
0.16	50	
0.40	1	

seem to be the same as those in the normal component.

3.4 Dust modeling

PB 8 is known to be very dusty (e.g. Lenzuni et al., 1989; Stasińska & Szczerba, 1999), which must influence the radiative processes in the nebula. Lenzuni et al. (1989) studied the IRAS measurements (25, 60 and 100 μm fluxes), and derived a dust temperature of $T_d = 85 \pm 0.4\text{K}$, an optical depth of $\tau(\text{Ly-c}) = 0.63$ and a dust-to-gas mass ratio of $\rho_d/\rho_g = 0.0123$ from a blackbody function fitted to the IRAS data. Similarly, Stasińska & Szczerba (1999) determined $T_d = 85\text{K}$, but $\rho_d/\rho_g = 0.0096$ from the broad band IRAS data. From the comparison of the mid-IR emission with a blackbody model of 150 K, Todt et al. (2010) suggested that it possibly contains a warm dust with different dust compositions. We notice that the models MC1 and MC2 cannot provide thermal effects to account for the *Spitzer* IR continuum, so a dust component is necessary to reproduce the spectral energy distribution (SED) of the nebula observed in the IR range. The third model (MC3) presented here treats dust properties of PB 8 using the dust radiative transfer features included in the MOCASSIN (Ercolano et al., 2005). Discrete grain sizes have been chosen based on the size range given by Mathis et al. (1977). The absence of the 9.7 μm amorphous silicate feature in the IR spectrum of PB 8 is commonly observed in O-rich circumstellar envelopes, which could imply this PN has a carbon-based dust. However, the strong features at 23.5, 27.5, and 33.8 μm are mostly attributed to crystalline silicates (Molster et al., 2002). The features seen at 6.2, 7.7, 8.6, and 11.3 μm are related to polycyclic aromatic hydrocarbons (PAHs) (García-Lario et al., 1999), together with broad features at 21 and 30 μm corresponding to a mixed chemistry having both O-rich and C-rich dust grains. The far-IR emission fluxes at 65 and 90 μm (Yamamura et al., 2010) could be related to relatively warm forsterite grains, which emit at a longer wavelength. The 65 μm emission may be related to a crystalline water-ice structure, although its presence cannot be confirmed at the moment.

The thermal IR emission of PB 8 was modeled by adding a mixed dust chemistry to the pure-gas photoionization model described in the previous sections.

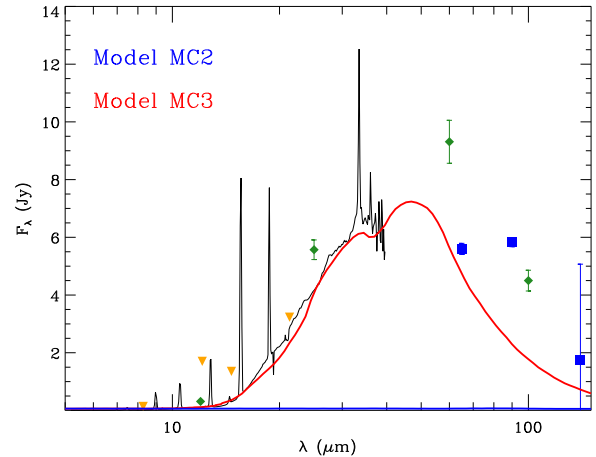


Figure 5. Observed *Spitzer* spectrum (black line) of PB 8 are compared with the continuum predicted by the model MC2 (blue line) and MC3 (red line). It also shows the photometric measurements for 12, 25, 60, and 100 μm (denoted by green diamonds) from IRAS (Helou & Walker, 1988), 8.3, 12.1, 14.7, and 21.34 μm (orange downward triangle) from MSX (Egan et al., 2003), and the far-IR measurements (blue squares) $F(65\text{ }\mu\text{m}) = 5.60 \pm 0.19$, $F(90\text{ }\mu\text{m}) = 5.83 \pm 0.16$, and $F(140\text{ }\mu\text{m}) = 1.74 \pm 3.33\text{ Jy}$ from AKARI/FIS (Yamamura et al., 2010). Note that the predicted nebular SED does not contain any nebular emission line fluxes.

We explored a number of grain sizes and species, which could provide a best-fitting curve to the *Spitzer* IR continuum (see Figure 5). As seen, the model MC2 cannot produce the IR continuum, whereas the model MC3 fairly produces it. We tried to match the far-IR emission flux at 65 μm , while the 140 μm flux is extremely uncertain, $F(140\text{ }\mu\text{m}) = 1.74 \pm 3.33\text{ Jy}$. The dust-to-gas mass ratio was varied until the best IR continuum flux was produced. Table 5 lists the dust parameters used for the final model of PB 8, the dust-to-gas ratio is given in Table 3. The geometry of the dust distribution is the same as the gas density distribution. The value of $\rho_d/\rho_g = 0.01$ found here is in agreement with Lenzuni et al. (1989). The final dust model incorporates two different grains, amorphous carbon and crystalline silicate with optical constants taken from Hanner (1988) and Jaeger et al. (1994), respectively. We also note that the nebular SED (shown in Figure 5), which is computed by MOCASSIN, does not contain any contributions from the nebular emission line fluxes.

For PB 8, Lenzuni et al. (1989) estimated a grain radius of 0.017 μm from the thermal balance equation under the assumption of the UV absorption efficiency $Q_{\text{UV}} = 1$. Stasińska & Szczerba (1999) argued that the method of Lenzuni et al. underestimates the grain radius, and one cannot derive the grain size in such a way. Our photoionization modeling implies that dust grains with a radius of 0.017 μm produce a very warm emission higher than $T_d = 85\text{K}$. The final dust model uses two discrete grain sizes, namely grain radii of 0.16 μm

(warm) and $0.40\ \mu\text{m}$ (cool), which can fairly reproduce the observed thermal infrared SED with wavelengths less than $80\ \mu\text{m}$. Smaller grain sizes can produce hot emission that increases the continuum at shorter wavelengths ($< 10\ \mu\text{m}$), whereas larger grain sizes add cooler emission that may depict as a rise in the continuum at longer wavelengths ($> 80\ \mu\text{m}$). Although the current two grain sizes can well reproduce the *Spitzer* SED of PB 8, the solutions may not be unique. A dust model with more than two grain sizes may also be possible, but it needs more computational simulations to find the best-fit model. Moreover, inhomogeneous dust distribution and viewing angles (see Figure 2 in Ercolano et al., 2005) can also change the predicted SED. As there is no information on the inclination of dust grains and their geometry, so we assumed that they follow the gas density distribution.

There is a discrepancy in fluxes with wavelengths higher than $80\ \mu\text{m}$, which could be attributed to a possible inhomogeneous dust distribution. We note that the band measurements with wavelengths higher $100\ \mu\text{m}$ could have high uncertainties, e.g., $F(140\ \mu\text{m}) = 1.74 \pm 3.33\ \text{Jy}$. We also note a small discrepancy for fluxes with wavelengths less than $15\ \mu\text{m}$, which could be related to the difference between the SL aperture ($3.7 \times 57\ \text{arcsec}^2$) and the LL aperture ($10.7 \times 168\ \text{arcsec}^2$) used for the SL spectrum ($5.2\text{--}14.5\ \mu\text{m}$) and the LL spectrum ($14.0\text{--}38.0\ \mu\text{m}$), and uncertainties in scaling up the SL spectrum (see Sec. 2). As both the LL and SL apertures covering some areas larger than the optical angular diameter of PB 8 ($7\ \text{arcsec}$), they could also be contaminated by the ISM surrounding the nebula.

4 RESULTS

4.1 Comparison of the emission-line fluxes

Table 6 lists the observed and predicted nebular emission line fluxes. Column 4 presents the observed, dereddened intensities of PB 8 from García-Rojas et al. (2009), relative to the intrinsic dereddened $\text{H}\beta$ flux, on a scale where $I(\text{H}\beta) = 100$. The ratios of predicted over observed values from the model MC1 are presented in Column 6. Columns 7–9 present the ratios of predicted over observed values for the normal component, the metal-rich component, and the entire nebula (normal+metal-rich) from the best-fitting model MC2. The same values obtained from the model MC3 are given in Columns 10–12. The majority of the CEL intensities predicted by model MC1 are in reasonable agreement with the observations. However, there are some large discrepancies between the prediction of model MC1 and the observations for ORLs. From the model MC2, it can be seen that the ORL discrepancy between model and observations can be explained by recombination processes of colder metal-rich inclusions embedded

in the global H-rich environments.

As seen in Table 6, the $[\text{N II}]\ \lambda 6584$ and $[\text{O III}]\ \lambda 5007$ line intensities predicted by the models MC1 and MC2 are in excellent agreement with the observations. As both the models MC2 and MC3 have exactly the same density distribution and chemical abundances, we can see how dust grains introduce a 10 percent increase in the $[\text{N II}]\ \lambda 6584$ line, which means that nitrogen abundance could be overestimated in some dusty nebulae. The H I line intensities as well as the majority of the He I line intensities are in reasonable agreement with the observations, discrepancies within 20 percent, apart from the $\text{He I}\ \lambda 3889$, $\lambda 5875$ and $\lambda 7065$ (around 30 percent). This could be due to high uncertainties of the recombination coefficients of the He I lines below $5000\ \text{K}$ (see Porter et al., 2012, 2013). The $[\text{O II}]\ \lambda 7319$ and $\lambda 7330$ doublets are underestimated by around 50 percent in the model MC1. Recombination processes can largely contribute to the observed fluxes of these lines, which can be estimated by the empirical equation given by Liu et al. (2000) (see equation 2).

There are discrepancies between the predicted intensities of $[\text{S II}]$ and $[\text{S III}]$ lines and the observed values. While the intensities of the $[\text{S II}]$ lines are predicted to be about 10–20 percent lower than the observations, the intensity of the $[\text{S III}]\ \lambda 6312$ line is calculated to be almost twice more than the observed value. Adjusting the sulfur abundance cannot help reproduce $[\text{S III}]$ lines, so these discrepancies could be related to either the atomic data or the physical conditions. The predicted intensities of $[\text{S II}]$ lines were calculated using S^+ collision strengths from Ramsbottom et al. (1996) incorporated into the CHIANTI database (V 7.0), which is currently used in MOCASSIN. Recently, new S^+ collision strengths were calculated by Tayal & Zatsarinny (2010), which ignored the effect of coupling to the continuum in their calculations, so their results were estimated to be accurate to about 30 percent or better. We note that the emissivities of $[\text{S II}]\ \lambda\lambda 6716, 6731$ lines calculated by the proEQUIB IDL Library³, which includes an IDL implementation of the Fortran program EQUIB (Howarth & Adams, 1981; Howarth et al., 2016), show that the collision strengths by Tayal & Zatsarinny (2010) make them about 8 percent lower at the given physical conditions. The predicted $[\text{S III}]$ line intensities are perhaps much more uncertain, as there seem to be some errors in the atomic data, as mentioned by Grieve et al. (2014). For example, the emissivity of $[\text{S III}]\ 18.68\ \mu\text{m}$ line calculated using the collision strengths from Tayal & Gupta (1999) is about 40 percent higher than the calculation made with Hudson et al. (2012) or Grieve et al. (2014). This issue might be related to the long-standing problem of the sulfur anomaly in PNe (see reviews by Henry et al., 2012).

³<https://github.com/equib/proEQUIB>

Table 6 Comparison of predictions from the models and the observations. The observed, dereddened intensities are in units such that $I(\text{H}\beta)=100$. Columns (6)–(12) give the ratios of predicted over observed values in each case.

Line	$\lambda_0(\text{\AA})$	Mult	I_{obs}	Err(%)	MC1	MC2			MC3		
						Normal	M-rich	Total	Normal	M-rich	Total
H, He recombination lines											
H β	4861.33	H4	100.000	5.0	1.000	0.772	0.228	1.000	0.771	0.229	1.000
H α	6562.82	H3	282.564	6.0	1.031	0.801	0.247	1.047	0.799	0.247	1.047
H γ	4340.47	H5	45.666	5.0	1.019	0.784	0.228	1.013	0.784	0.229	1.013
H δ	4101.74	H6	24.285	5.0	1.057	0.813	0.235	1.048	0.813	0.236	1.049
H I	3970.07	H7	14.466	6.0	1.089	0.838	0.242	1.080	0.837	0.243	1.080
H I	3835.39	H9	6.784	6.0	1.069	0.822	0.238	1.060	0.822	0.239	1.061
He I	3888.65	2	19.892	6.0	0.702	0.531	0.235	0.766	0.532	0.236	0.768
He I	7065.28	10	4.265	7.0	0.752	0.552	0.202	0.754	0.555	0.203	0.758
He I	5875.64	11	17.127	6.0	1.089	0.852	0.473	1.325	0.850	0.473	1.323
He I	4471.47	14	6.476	5.0	1.014	0.787	0.411	1.199	0.786	0.412	1.198
He I	4026.21	18	3.116	6.0	0.976	0.757	0.366	1.123	0.756	0.367	1.123
He I	7281.35	45	0.815	8.0	1.126	0.842	0.339	1.181	0.844	0.340	1.185
He I	6678.15	46	5.233	6.0	1.020	0.802	0.432	1.233	0.799	0.432	1.231
He I	4921.93	48	1.737	5.0	1.014	0.790	0.402	1.191	0.788	0.403	1.191
Heavy-element recombination lines											
C II	6578.05	2	0.545	9.0	0.575	0.438	0.126	0.563	0.437	0.126	0.563
C II	7231.34	3	0.234	17.0	1.088	0.840	0.257	1.096	0.837	0.257	1.094
C II	7236.42	3	0.464	10.0	0.988	0.762	0.233	0.995	0.760	0.233	0.993
C II	4267.15	6	0.781	7.0	0.857	0.670	0.218	0.888	0.667	0.218	0.885
N II	5666.64	3	0.192	25.0	0.114	0.048	0.683	0.731	0.048	0.685	0.732
N II	5676.02	3	0.084	:	0.116	0.049	0.693	0.741	0.048	0.694	0.743
N II	5679.56	3	0.260	18.0	0.157	0.066	0.940	1.006	0.066	0.942	1.007
N II	4601.48	5	0.099	21.0	0.073	0.031	0.420	0.451	0.030	0.421	0.452
N II	4607.16	5	0.083	25.0	0.070	0.029	0.400	0.429	0.029	0.401	0.430
N II	4613.87	5	0.063	30.0	0.069	0.029	0.395	0.424	0.029	0.396	0.424
N II	4621.39	5	0.085	24.0	0.068	0.028	0.390	0.418	0.028	0.391	0.419
N II	4630.54	5	0.289	10.0	0.075	0.031	0.429	0.460	0.031	0.430	0.461
N II	4643.06	5	0.122	18.0	0.059	0.025	0.338	0.362	0.025	0.339	0.363
N II	4994.37	24	0.099	21.0	0.066	0.028	0.420	0.448	0.028	0.421	0.449
N II	5931.78	28	0.151	30.0	0.045	0.019	0.284	0.303	0.019	0.285	0.304
N II	5941.65	28	0.115	:	0.110	0.047	0.696	0.743	0.046	0.697	0.743
O II	4638.86	1	0.206	12.0	0.181	0.197	0.527	0.724	0.196	0.527	0.723
O II	4641.81	1	0.380	8.0	0.248	0.270	0.720	0.990	0.268	0.721	0.989
O II	4649.13	1	0.458	8.0	0.391	0.426	1.136	1.562	0.423	1.137	1.561
O II	4650.84	1	0.221	12.0	0.169	0.184	0.491	0.675	0.183	0.491	0.674
O II	4661.63	1	0.222	12.0	0.215	0.234	0.624	0.858	0.232	0.625	0.857
O II	4676.24	1	0.184	13.0	0.218	0.237	0.633	0.870	0.236	0.633	0.869
O II	4319.63	2	0.081	26.0	0.364	0.397	1.067	1.465	0.395	1.068	1.463
O II	4336.83	2	0.054	36.0	0.161	0.176	0.472	0.648	0.175	0.472	0.647
O II	4349.43	2	0.197	13.0	0.346	0.378	1.016	1.395	0.376	1.017	1.393
O II	3749.48	3	0.281	11.0	0.132	0.143	0.375	0.518	0.142	0.376	0.518
O II	4414.90	5	0.036	:	0.489	0.524	1.275	1.799	0.521	1.278	1.799
O II	4416.97	5	0.090	24.0	0.109	0.116	0.283	0.399	0.116	0.284	0.399
O II	4072.15	10	0.265	11.0	0.331	0.363	0.987	1.350	0.360	0.988	1.348
O II	4075.86	10	0.275	11.0	0.460	0.505	1.374	1.879	0.501	1.375	1.876
O II	4085.11	10	0.086	26.0	0.190	0.209	0.568	0.776	0.207	0.568	0.775
O II	4121.46	19	0.163	16.0	0.063	0.069	0.191	0.260	0.069	0.191	0.260
O II	4132.80	19	0.202	13.0	0.099	0.109	0.301	0.410	0.108	0.301	0.410
O II	4153.30	19	0.250	12.0	0.115	0.126	0.348	0.474	0.125	0.348	0.473
O II	4110.79	20	0.147	17.0	0.060	0.066	0.182	0.248	0.066	0.182	0.248
O II	4119.22	20	0.087	25.0	0.374	0.411	1.133	1.544	0.408	1.133	1.541
O II	4699.22	25	0.026	:	0.093	0.103	0.283	0.386	0.102	0.283	0.385
O II	4906.81	28	0.096	21.0	0.096	0.105	0.289	0.394	0.104	0.289	0.394
O II	4924.53	28	0.154	15.0	0.101	0.111	0.307	0.418	0.111	0.307	0.417

Line	$\lambda_0(\text{\AA})$	Mult	I_{obs} Err(%)		MC1	MC2			MC3		
						Normal	M-rich	Total	Normal	M-rich	Total
Collisionally excited lines											
[N II] ^d	5754.64	3F	0.346	14.0	0.495	0.186	0.506	0.692	0.199	0.509	0.708
[N II]	6548.03	1F	7.667	6.0	0.926	0.393	0.613	1.006	0.418	0.631	1.048
[N II]	6583.41	1F	22.318	6.0	0.972	0.412	0.643	1.055	0.438	0.662	1.100
[O II]	3726.03	1F	17.103	6.0	0.897	0.947	0.061	1.008	1.035	0.065	1.100
[O II]	3728.82	1F	9.450	6.0	0.782	0.813	0.044	0.857	0.890	0.047	0.936
[O II] ^d	7318.92	2F	0.227	18.0	0.530	0.491	0.538	1.029	0.546	0.539	1.085
[O II] ^d	7319.99	2F	0.811	8.0	0.451	0.418	0.536	0.954	0.465	0.538	1.003
[O II] ^d	7329.66	2F	0.387	12.0	0.518	0.480	0.537	1.017	0.535	0.539	1.074
[O II] ^d	7330.73	2F	0.471	10.0	0.419	0.388	0.536	0.924	0.432	0.537	0.969
[O III]	4363.21	2F	0.528	7.0	1.733	0.927	0.007	0.935	0.995	0.008	1.003
[O III]	4958.91	1F	116.957	5.0	1.130	0.858	0.137	0.995	0.886	0.143	1.028
[O III]	5006.84	1F	348.532	5.0	1.132	0.859	0.137	0.996	0.887	0.143	1.030
[Ne II]	12.82 μm		24.370	...	0.516	0.696	0.209	0.905	0.716	0.207	0.923
[Ne III]	3868.75	1F	19.164	6.0	1.131	0.784	0.006	0.790	0.816	0.006	0.822
[Ne III]	3967.46	1F	5.689	6.0	1.147	0.795	0.006	0.801	0.828	0.006	0.835
[Ne III]	15.55 μm		110.660	...	1.006	1.054	0.203	1.257	1.050	0.206	1.255
[Ne III]	36.02 μm		7.360	...	1.275	1.331	0.236	1.566	1.326	0.239	1.565
[S II]	4068.60	1F	0.223	:	1.004	0.699	0.011	0.710	0.772	0.012	0.784
[S II]	6716.47	2F	0.957	7.0	0.978	0.742	0.026	0.769	0.809	0.028	0.837
[S II]	6730.85	2F	1.441	7.0	1.010	0.773	0.032	0.805	0.843	0.034	0.877
[S III]	6312.10	3F	0.639	9.0	3.617	1.984	0.015	2.000	2.109	0.016	2.126
[S III]	18.68 μm		54.820	...	2.495	1.974	0.393	2.367	2.008	0.395	2.403
[S III]	33.65 μm		30.360	...	2.076	1.624	0.225	1.849	1.652	0.226	1.878
[Cl III]	5517.71	1F	0.366	14.0	0.940	0.711	0.014	0.725	0.736	0.014	0.750
[Cl III]	5537.88	1F	0.366	14.0	1.054	0.806	0.020	0.826	0.834	0.021	0.855
[Ar III]	7135.78	1F	15.477	7.0	1.048	0.775	0.035	0.809	0.796	0.035	0.831
[Ar III]	7751.10	2F	3.493	7.0	1.113	0.822	0.037	0.859	0.845	0.038	0.883
[Ar III]	8.99 μm		14.970	...	1.657	1.483	0.351	1.834	1.490	0.351	1.841
$H\beta^a/10^{-12} \text{ erg cm}^{-2} \text{ s}^{-1}$			19.7	13.0	0.884	0.863	0.255	1.118	0.856	0.254	1.110
$\tau(\text{H I})^b$					0.556			0.581			0.651
$\tau(\text{He I})^c$					0.336			0.343			0.422

^a The intrinsic $H\beta$ line flux of the entire nebula.

^b Optical depth at the H I photoionization threshold (13.6 eV).

^c Optical depth at the He I photoionization threshold (24.6 eV).

^d Recombination contribution estimated by equations (1) and (2) included in the predicted lines.

The predicted intensities of the [Ar III] $\lambda\lambda 7136, 7751$ lines are in agreement with the observations, discrepancies within 20 percent, however, the IR fine-structure [Ar III] 8.99 μm line is predicted to be about 80 percent higher. We used Ar^{2+} collision strengths from Galavis et al. (1995) used by the CHIANTI database (V 7.0). There is another set for Ar^{2+} collision strengths (Munoz Burgos et al., 2009) whose predictions are significantly different and need to be examined carefully. We notice that the emissivities of [Ar III] $\lambda\lambda 7136, 7751$ lines predicted by proEQUIB with the collision strengths from Munoz Burgos et al. (2009) show a discrepancy of about 9 percent in comparison to those calculated with Galavis et al. (1995), whereas there is a 30 percent difference in the [Ar III] 8.99 μm emissivity calculated with the different atomic data.

The predicted [Ne II] $\lambda 12.82 \mu\text{m}$ and [Ne III] $\lambda\lambda 3869, 3967$ line intensities do not show high discrepancies (less than 20 percent), nevertheless, the calculated intensities of [Ne II] $\lambda\lambda 15.55, 36.02 \mu\text{m}$ lines have

discrepancies about 26 and 57 percent. The predicted [Cl III] $\lambda\lambda 5518, 5538$ lines are in agreement with the observations, discrepancies less than 25 percent.

Although the [O III] $\lambda 4363$ auroral line is perfectly matched by the model MC3 and discrepancies remain less than 10 percent in the model MC2, there is a notable discrepancy in the [N II] $\lambda 5755$ auroral line. This could be due to excitation by continuum fluorescence and/or recombination process. Bautista (1999) found that the [N I] $\lambda\lambda 5198, 5200$ lines are efficiently affected by fluorescence excitation in many objects, while [O I] lines were found to be sensitive to fluorescence in colder regions ($\leq 5000 \text{ K}$) or very high radiation fields. Nevertheless, this PN is not known to be surrounded by a photo-dissociation region (PDR) that is responsible for the fluorescence excitation. We notice that García-Rojas et al. (2009) observed the brightest part of the nebula, and excluded the central star contamination and the surrounding potential PDR. Moreover, the absences of the [O I] $\lambda\lambda 6300, 6364$ lines emitted by neutral

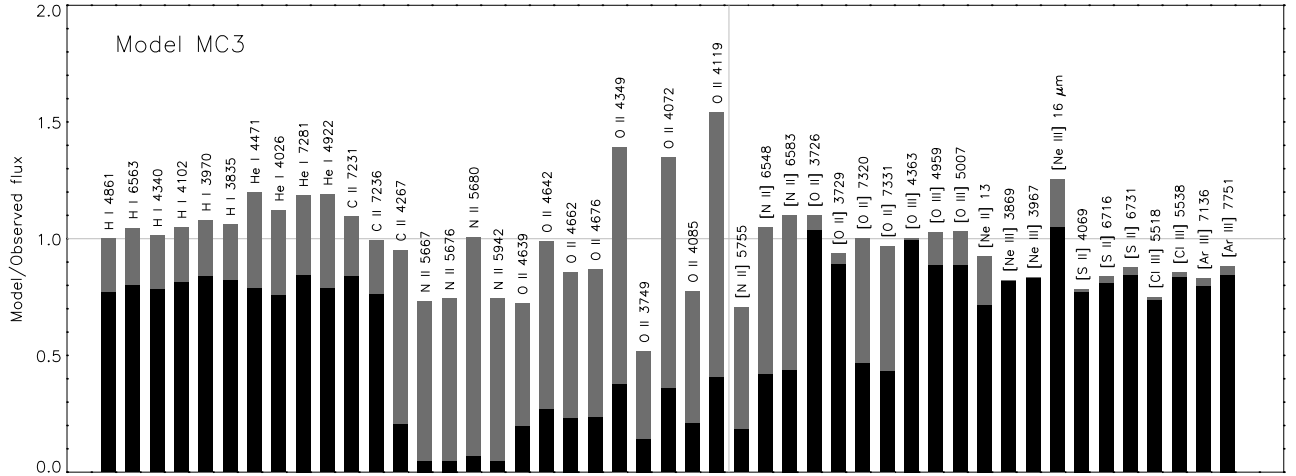


Figure 6. The predicted over observed flux ratio for the bi-abundance model MC3. The relative contributions of the normal and the metal-rich components to each line flux are shown by black and grey parts, respectively.

O^0 ion and the $[N\text{ I}]\lambda\lambda 5198,5200$ lines emitted by neutral N^0 ion in the spectrum presented by García-Rojas et al. (2009) exclude any possibilities of the fluorescence contamination. Hence, there is no strong evidence for any possible fluorescence contributions to the observed fluxes. Alternatively, the recombination contribution to $[N\text{ II}]$ auroral lines may have some implications, which can be estimated for low-density uniform nebular media (see e.g. Liu et al., 2000).

The recombination contribution to the $[N\text{ II}]\lambda 5755$ line and the $[O\text{ II}]\lambda\lambda 7320,7330$ doublet can be estimated as follows (Liu et al., 2000):

$$\frac{I_R(\lambda 5755)}{I(\text{H}\beta)} = 3.19 t^{0.30} \left(\frac{N^{2+}}{H^+} \right)_{\text{ORLs}}, \quad (1)$$

$$\frac{I_R(\lambda 7320 + \lambda 7330)}{I(\text{H}\beta)} = 9.36 t^{0.44} \left(\frac{O^{2+}}{H^+} \right)_{\text{ORLs}}, \quad (2)$$

where $t \equiv T_e/10^4$ is the electron temperature in 10^4 K from Tables 7 and 8 and $(N^{2+}/H^+)_{\text{ORLs}}$ and $(O^{2+}/H^+)_{\text{ORLs}}$ derived from Tables 3, 9 and 10. The recombination contributions to the $[N\text{ II}]\lambda 5755$ auroral line are estimated to be about 12 percent in the model MC1 and 48 percent in the models MC2 and MC3 (including contributions from the metal-rich inclusions). As MOCASSIN does not currently estimate the recombination contributions to the auroral lines (due to the lack of atomic data), we empirically calculated them with equations (1) and (2) and included them in the $[N\text{ II}]\lambda 5755$ line and the $[O\text{ II}]\lambda\lambda 7320,7330$ doublet in Tables 6. We see that the $[N\text{ II}]\lambda 5755$ auroral line in the model MC3 show better agreement, but about 30 percent lower. The uncertainty of this faint line, 14 percent reported by García-Rojas et al. (2009), which could

be even higher, may explain this discrepancy. Additionally, it is extremely difficult to evaluate the recombination contribution in the presence of inhomogeneous condensations. The collisional de-excitations of very dense clumps in the nebula can suppress the $\lambda\lambda 6548,6584$ nebular lines, but not the auroral lines (Viegas & Clegg, 1994), so the discrepancy between the model and the observation could be related due to unknown inhomogeneous condensations and high uncertainties in the recombination atomic data at low temperatures (i.e., below 5000 K in a dense clump). Similarly, the recombination contribution to the $[O\text{ II}]\lambda\lambda 7320,7330$ doublets are estimated to be about 15 percent in the model MC1 and 53 percent in the models MC2 and MC3. As you see, the predicted $[O\text{ II}]\lambda\lambda 7320,7330$ doublets are in excellent agreement with the observations.

The intensities of the ORLs predicted by the model MC2 and MC3, both bi-abundance models, can be compared to the observed values in Table 6. Figure 6 compares the predicted over observed flux ratio for the model MC3, and shows the relative contributions of the normal and the metal-rich components to each emission-line flux. The agreement between the ORL intensities predicted by the two latter models and the observations is better than those derived from the first model (MC1). The majority of the $O\text{ II}$ lines with strong intensities are in reasonable agreement with the observations, with discrepancies below 40 percent, except for $\lambda 4649.13$, $\lambda 3749.48$, $\lambda 4075.86$, $\lambda 4132.80$ and $\lambda 4153.30$. The well-measured $N\text{ II}\lambda 5666.64$, $\lambda 5676.02$ and $\lambda 5679.56$ lines are in good agreement with the observations, and discrepancies are less than 30 percent. There are some discrepancies in some $O\text{ II}$ ORLs

Table 7 Mean electron temperatures (K) weighted by ionic species for the entire nebula. For each element the first row is for MC1 and the second row is for MC2.

El.	Ion						
	I	II	III	IV	V	VI	VII
H	7746	7625					
	6647	6584					
He	7746	7625	7595				
	6655	6584	6784				
C	7829	7741	7621	7468	7431	7625	7625
	6806	6673	6580	6549	6631	6584	6584
N	7834	7746	7617	7468	7431	7625	7625
	6883	6772	6567	6439	6565	6584	6584
O	7860	7746	7613	7566	7625	7625	7625
	7176	6692	6568	6618	6584	6584	6584
Ne	7812	7720	7601	7564	7625	7625	7625
	6602	6599	6579	6764	6584	6584	6584
S	7855	7783	7685	7541	7411	7390	7625
	6760	6676	6632	6497	6453	6572	6584
Cl	7836	7748	7635	7503	7467	7625	7625
	6747	6658	6598	6408	6612	6584	6584
Ar	7846	7766	7659	7535	7490	7625	7625
	6699	6606	6588	6570	6684	6584	6584

(e.g. $\lambda 4416.97$, $\lambda 4121.46$, $\lambda 4906.81$) and N II ORLs (e.g. $\lambda 4601.48$, $\lambda 4613.87$, $\lambda 5931.78$), which have weak intensities and higher uncertainties (20–30 percent). However, as seen in Figure 6, the model MC3 has significant improvements in predicting the O II and N II lines having intensities stronger than other ORLs. Particularly, the bi-abundance models MC2 and MC3 provide better predictions for the O II ORLs from the V1 multiplet and the N II ORLs from the V3 multiplet, which have the reliable atomic data. Comparing Figure 6 with Fig. 15 in Yuan et al. (2011) demonstrates that our bi-abundance models of PB 8, similar to the photoionization model of NGC 6153, better predict the observed intensities of the N II and O II ORLs. The models also reproduce the C II ORLs with discrepancies about 10 percent, except the C II $\lambda 6578$ line. The C II $\lambda 4267.2$ line is stronger than the other C II lines, and it is not blended with any nearby O II ORLs. The C II $\lambda 6578$ line may be blended with nearby lines, so its measured line strength may be uncertainty.

4.2 Thermal structure

Table 7 lists the mean electron temperatures of the entire nebula in the models MC1 and MC2 weighted by ionic species, from the neutral (I) to the highly ionized ions (VII). The definition for the weighted-mean temperatures was given in Ercolano et al. (2003b). The value of $T_e(\text{N II}) = 7746$ K predicted by the model MC1 is about 1150 K lower than the value of $T_e(\text{N II}) = 8900 \pm 500$ K empirically derived from CELs by García-Rojas et al. (2009). This could be due to recombination contributions to the auroral line. The recombination contribu-

Table 8 Mean electron temperatures (K) weighted by ionic species for the nebula obtained from the photoionization model MC3. For each element the first row is for the normal component, the second row is for the H-poor component, and the third row is for the entire nebula.

El.	Ion						
	I	II	III	IV	V	VI	VII
H	7298	7097					
	4341	4309					
	6719	6640					
He	7307	7097	7054				
	4343	4309	4310				
	6726	6640	6843				
C	7436	7295	7088	6795	6739	7098	7098
	4361	4342	4307	4252	4253	4309	4309
	6886	6742	6635	6491	6640	6641	6641
N	7460	7315	7077	6796	6738	7098	7098
	4363	4344	4306	4257	4258	4309	4309
	6959	6840	6622	6414	6580	6641	6641
O	7507	7319	7064	6989	7098	7098	7098
	4364	4346	4302	4302	4309	4309	4309
	7250	6762	6621	6671	6641	6641	6641
Ne	7414	7260	7042	6988	7098	7098	7098
	4361	4340	4294	4295	4309	4309	4309
	6690	6671	6630	6819	6641	6641	6641
S	7466	7349	7186	6937	6713	6678	7098
	4365	4349	4324	4276	4243	4243	4309
	6848	6751	6694	6541	6435	6597	6641
Cl	7444	7302	7113	6875	6720	6721	7098
	4361	4343	4312	4261	4241	4245	4309
	6832	6731	6656	6444	5640	6241	6641
Ar	7468	7336	7148	6929	6861	7098	7098
	4366	4349	4317	4267	4267	4309	4309
	6783	6680	6647	6618	6737	6641	6641

tion estimated (using Eq. 1 in Liu et al., 2000) about 12 percent in the model MC1 is much lower to explain the measured intensity of the [N II] $\lambda 5755$ line. However, the model MC2 predicts the [N II] $\lambda 5755$ line to be 40 percent higher than the value derived from the model MC1 (see recombination contribution estimated by Eq. 1 in Table 6). We also notice that the [N II] temperature is roughly equal to the [O III] temperature in low excitation PNe (Kingsburgh & Barlow, 1994), so the empirical value of the [N II] electron temperature derived by García-Rojas et al. (2009) is difficult to be explained. The temperature $T_e(\text{O II}) = 7746$ K predicted by the model MC1 is about 670 K higher than $T_e(\text{O II}) = 7050 \pm 400$ K empirically derived by García-Rojas et al. (2009), while $T_e(\text{O II}) = 6692$ K predicted by the model MC2 is about 360 K lower than the empirical value. Moreover, the temperature of [O III] calculated from the model MC1, $T_e(\text{O III}) = 7613$ K, is about 710 K higher the empirical result of $T_e(\text{O III}) = 6900 \pm 150$ K, whereas $T_e(\text{O III}) = 6568$ K predicted by the model MC2 is about 330 K lower the empirical value.

Table 8 presents the electron temperatures of the dif-

ferent components of the model MC3 weighted by ionic abundances, as well as the mean temperatures of the entire nebula. The first entries for each element are for the normal abundance plasma, the second entries are for the metal-rich inclusion, and the third entries are for the entire nebula (including both the normal and the H-poor components). It can be seen that the temperatures weighted by ionic abundances in the two different components of the nebula are very different. The electron temperatures separately weighted by the ionic species of the metal-rich inclusions were much lower than those from the normal part. The temperature of $T_e(\text{N II}) = 7315 \text{ K}$ predicted by the normal component of the model MC3 is about 1590 K lower than the value empirically derived. However, $T_e(\text{O II}) = 7319 \text{ K}$ and $T_e(\text{O III}) = 7064 \text{ K}$ obtained by the normal component of the model MC3 are in reasonable agreement with the values empirically derived by García-Rojas et al. (2009). We see that $T_e(\text{He I}) = 4309 \text{ K}$ weighted by the metal-rich component of the model MC3 is lower than the empirical value, $T_e(\text{He I}) = 6250 \pm 150 \text{ K}$ (García-Rojas et al., 2009), whereas $T_e(\text{He I}) = 6640 \text{ K}$ weighted by the whole nebula is about 390 K higher the empirical value. Moreover, $T_e(\text{H I}) = 4309 \text{ K}$ weighted by the metal-rich component and $T_e(\text{H I}) = 6640 \text{ K}$ weighted by the whole nebula are reasonably in the range of $T_e(\text{H I}) = 5100_{-900}^{+1300} \text{ K}$ empirically derived from the Balmer Jump to H11 flux ratio (García-Rojas et al., 2009). We take no account for the interaction between the two components, namely normal and metal-rich, which could also lead to a temperature variation. Note that the radiative transfer in a neutral region is not currently supported by MOCASSIN, so the code only estimates temperatures that likely correspond to a potential narrow transition region between ionized and neutral regions for a radiation-bounded object. Neutral elements in this PN are negligible (see Table 9), so the temperatures of the neutral species listed in Table 8 do not have any significant physical meaning. We also see that the two components have a local thermal pressure ratio of $P(\text{metal-rich})/P(\text{normal}) \sim 1.1$, which means each metal-rich cell is in pressure equilibrium with its surrounding normal gas. The higher thermal pressure forces the dense, metal-rich knots to expand and reduce their density and temperature during the evolution phase of the nebula.

4.3 Fractional ionic abundances

Table 9 lists the volume-averaged fractional ionic abundances from the neutral (I) to the highly ionized ions (VII) calculated from the three models, where, the first entries for each element are for the chemically homogeneous model MC1, the second entries are for the bi-abundance model MC2, and the third entries are the dusty bi-abundance model MC3. The definition for the

volume-averaged fractional ionic abundances was given in Ercolano et al. (2003b). We see that both hydrogen and helium are fully singly-ionized, i.e. neutrals are almost zero percent in the three models. It can be seen that the ionization structure in MC2 is in reasonable agreement with MC1. The elemental oxygen largely exists as O^{2+} with 91 percent and then O^+ with 9 percent in the model MC1, whereas O^{2+} is about 87 percent and then O^+ is about 13 percent in the model MC2. Moreover, the elemental nitrogen largely exists as N^{2+} with 93 percent and then N^+ with 7 percent in the model MC1, whereas N^{2+} is about 91 percent and then N^+ is about 9 percent in the model MC2. The O^+/O ratio is about 1.4–1.6 times higher than the N^+/N ratio, which is in disagreement with the general assumption of $\text{N}/\text{N}^+ = \text{O}/\text{O}^+$ in the ionization correction factor (*icf*) method by Kingsburgh & Barlow (1994), introducing errors to empirically derived elemental abundances. Our $(\text{N}^+/\text{N})/(\text{O}^+/\text{O})$ ratio is in agreement with the value of 0.6–0.7 predicted by the photoionization model of NGC 7009 implemented using MOCASSIN (Gonçalves et al., 2006). While the assumption $\text{N}/\text{N}^+ = \text{O}/\text{O}^+$ overestimates the N/H elemental abundance, the new *icf*(N/O) calculated using 1-D photoionization modeling provides a better agreement (Delgado-Inglada et al., 2014). Moreover, the O^{2+}/O ratio is about 1.1–1.2 higher than the Ne^{2+}/Ne ratio, in reasonable agreement with the assumption for the *icf*(Ne). The ionic fraction of S, Cl and Ar predicted by MC2 are approximately about the values calculated by MC1. The small discrepancies in fractional ionic abundances between MC1 and MC2 can be explained by a small fraction of the metal-rich structures included in MC2.

The volume-averaged fractional ionic abundances calculated from the model MC2 are listed in Table 10, the upper entries for each element in the table are for the normal component and the lower entries are for the metal-rich component of the nebula. It can be seen that the model MC2 predict different ionic fractions of O^+ for the two components of the nebula, whereas roughly the same value for N^+ . The O^+/O ratios in the metal-rich component are about 20 percent higher than those in the normal component. This means that that the ionization correction factors (*icf*) from CELs are not entirely accurate for deriving the elemental abundances from ORLs as adopted by some authors (see e.g. Wang & Liu, 2007).

5 CONCLUSIONS

Three photoionization models have been constructed for the planetary nebula PB 8, a chemically homogeneous model, a bi-abundance model and a dusty bi-abundance model. Our intention was to construct a model that well reproduce the observed emission-lines and ther-

Table 9 Fractional ionic abundances obtained from the photoionization models. For each element the first row is for MC1, the second row is for MC2 and the third row is for MC3.

Element	Ion						
	I	II	III	IV	V	VI	VII
H	6.88(-4)	9.99(-1)					
	8.23(-4)	9.99(-1)					
	8.59(-4)	9.99(-1)					
He	1.91(-3)	9.98(-1)	1.62(-12)				
	2.39(-3)	9.98(-1)	1.38(-12)				
	2.47(-3)	9.98(-1)	1.39(-12)				
C	1.19(-5)	4.15(-2)	9.56(-1)	2.39(-3)	2.70(-16)	1.00(-20)	1.00(-20)
	1.63(-5)	5.03(-2)	9.48(-1)	1.86(-3)	1.91(-16)	1.00(-20)	1.00(-20)
	1.75(-5)	5.18(-2)	9.46(-1)	1.71(-3)	1.75(-16)	1.00(-20)	1.00(-20)
N	1.60(-5)	6.82(-2)	9.28(-1)	3.40(-3)	6.86(-16)	1.00(-20)	1.00(-20)
	2.51(-5)	8.50(-2)	9.12(-1)	2.92(-3)	5.41(-16)	1.00(-20)	1.00(-20)
	2.69(-5)	8.74(-2)	9.10(-1)	2.80(-3)	5.21(-16)	1.00(-20)	1.00(-20)
O	6.40(-5)	9.40(-2)	9.06(-1)	2.00(-13)	1.00(-20)	1.00(-20)	1.00(-20)
	1.06(-4)	1.31(-1)	8.68(-1)	1.82(-13)	1.00(-20)	1.00(-20)	1.00(-20)
	1.19(-4)	1.36(-1)	8.64(-1)	1.81(-13)	1.00(-20)	1.00(-20)	1.00(-20)
Ne	1.06(-4)	2.02(-1)	7.97(-1)	7.74(-14)	1.00(-20)	1.00(-20)	1.00(-20)
	1.78(-4)	2.61(-1)	7.39(-1)	6.04(-14)	1.00(-20)	1.00(-20)	1.00(-20)
	1.87(-4)	2.65(-1)	7.35(-1)	6.03(-14)	1.00(-20)	1.00(-20)	1.00(-20)
S	3.01(-7)	4.72(-3)	5.81(-1)	4.13(-1)	1.90(-3)	8.26(-16)	1.00(-20)
	4.46(-7)	6.14(-3)	6.36(-1)	3.56(-1)	1.46(-3)	5.63(-16)	1.00(-20)
	4.87(-7)	6.46(-3)	6.42(-1)	3.50(-1)	1.42(-3)	5.48(-16)	1.00(-20)
Cl	2.68(-6)	1.85(-2)	8.91(-1)	9.02(-2)	9.99(-15)	1.00(-20)	1.00(-20)
	3.79(-6)	2.22(-2)	8.97(-1)	8.09(-2)	7.66(-15)	1.00(-20)	1.00(-20)
	4.12(-6)	2.30(-2)	8.96(-1)	8.09(-2)	5.00(-7)	1.47(-19)	1.00(-20)
Ar	4.47(-7)	4.11(-3)	7.21(-1)	2.75(-1)	1.56(-13)	1.00(-20)	1.00(-20)
	7.85(-7)	5.95(-3)	7.72(-1)	2.22(-1)	1.11(-13)	1.00(-20)	1.00(-20)
	8.43(-7)	6.12(-3)	7.72(-1)	2.22(-1)	1.12(-13)	1.00(-20)	1.00(-20)

Table 10 Fractional ionic abundances obtained from the photoionization model MC2. For each element the first row is for the normal component and the second row is for the H-poor component.

Element	Ion						
	I	II	III	IV	V	VI	VII
H	7.86(-4)	9.99(-1)					
	1.01(-3)	9.99(-1)					
He	2.28(-3)	9.98(-1)	1.53(-12)				
	2.93(-3)	9.97(-1)	6.49(-13)				
C	1.59(-5)	4.86(-2)	9.49(-1)	2.05(-3)	2.22(-16)	1.00(-20)	1.00(-20)
	1.87(-5)	5.89(-2)	9.40(-1)	9.20(-4)	3.12(-17)	1.00(-20)	1.00(-20)
N	2.49(-5)	8.49(-2)	9.12(-1)	3.06(-3)	6.13(-16)	1.00(-20)	1.00(-20)
	2.60(-5)	8.55(-2)	9.12(-1)	2.20(-3)	1.73(-16)	1.00(-20)	1.00(-20)
O	1.16(-4)	1.27(-1)	8.73(-1)	1.92(-13)	1.00(-20)	1.00(-20)	1.00(-20)
	5.74(-5)	1.55(-1)	8.45(-1)	1.31(-13)	1.00(-20)	1.00(-20)	1.00(-20)
Ne	1.60(-4)	2.47(-1)	7.53(-1)	6.77(-14)	1.00(-20)	1.00(-20)	1.00(-20)
	2.72(-4)	3.32(-1)	6.68(-1)	2.29(-14)	1.00(-20)	1.00(-20)	1.00(-20)
S	4.20(-7)	5.83(-3)	6.29(-1)	3.64(-1)	1.59(-3)	6.56(-16)	1.00(-20)
	5.74(-7)	7.74(-3)	6.75(-1)	3.17(-1)	7.82(-4)	8.85(-17)	1.00(-20)
Cl	3.59(-6)	2.13(-2)	8.97(-1)	8.13(-2)	8.59(-15)	1.00(-20)	1.00(-20)
	4.84(-6)	2.69(-2)	8.94(-1)	7.89(-2)	2.87(-15)	1.00(-20)	1.00(-20)
Ar	7.21(-7)	5.50(-3)	7.60(-1)	2.35(-1)	1.26(-13)	1.00(-20)	1.00(-20)
	1.11(-6)	8.25(-3)	8.37(-1)	1.55(-1)	3.19(-14)	1.00(-20)	1.00(-20)

mal structure determined from the plasma diagnostics. A powerlaw radial density profile was adopted for the spherical nebula distribution based on the radiation-hydrodynamics simulations. The density model parameters were adjusted to reproduce the total $H\beta$ intrinsic line flux of the nebula, and the mean electron density empirically derived from the CELs (García-Rojas et al., 2009). We have used the non-LTE model atmosphere derived by Todt et al. (2010) for temperature $T_{\text{eff}} = 52 \text{ kK}$ and luminosity $L_* = 6000L_{\odot}$. This ionizing source well reproduced the nebular observed $H\beta$ absolute flux, as well as the $[\text{O III}] \lambda 5007$ line flux, at the distance of 4.9 kpc.

Our initial model reproduces the majority of CELs and the thermal structure, but large discrepancies exist in the observed ORLs from heavy element ions. It is found that a chemically homogeneous model cannot consistently explain the ORLs observed in the nebular spectrum. We therefore intended to address the cause of the heavily underestimated ORLs. Following the hypothesis of the bi-abundance model by Liu et al. (2000), a small fraction of metal-rich inclusions was introduced into the second model. The heavy element ORLs are mostly emitted from the metal-rich structures embedded in the dominant diffuse warm plasma of normal abundances. The agreement between the ORL intensities predicted by the model MC2 and the observations is better than the first model (MC1). The metal-rich inclusions occupying 5.6 percent of the total volume of the nebula, and are about 1.7 times cooler and denser than the normal composition nebula. The O/H and N/H abundance ratios in the metal-rich inclusions are ~ 1.0 and 1.7 dex larger than the diffuse warm nebula, respectively. The mean electron temperatures predicted by MC2 are lower than those from MC1, which is because of the cooling effects of the metal-rich inclusions. The results indicate that a bi-abundance model can naturally explain the heavily underestimated ORLs in the chemically homogeneous model. Therefore, the metal-rich inclusions may solve the problem of ORL/CEL abundance discrepancies. However, the model MC2 cannot explain the thermal SED of the nebula observed with the *Spitzer* spectrograph. In our final model, we have incorporated a dual dust chemistry consisting of two different grains, amorphous carbon and crystalline silicate, and discrete grain radii. It is found that a dust-to-gas ratio of 0.01 by mass for the whole nebula can roughly reproduce the observed IR continuum.

The PN PB 8 shows moderate ADFs (~ 1.9 – 2.6 ; García-Rojas et al., 2009), which are typical of most PNe (see e.g. Liu, 2006). Previously, the bi-abundance model were only examined in two PNe with extremely large ADFs: Abell 30 (Ercolano et al., 2003c) and NGC 6153 (Yuan et al., 2011). In Abell 30, Ercolano et al. (2003c) used a metal-rich core whose density is about six times larger than the surrounding nebula.

In NGC 6153, Yuan et al. (2011) used super-metal-rich knots distributed in the inner region of the nebula. In the present study, we adopted a bi-abundance model whose metal-rich knots are homogeneously distributed inside the diffuse warm nebula, and are associated with a gas-filling factors of 0.056. To reproduce the spectrum of PB 8, it is not require to have extremely dense and super-metal-rich knots, since the ORLs do not correspond to very cold temperatures and extremely large ADFs such as Abell 30 and NGC 6153. We should mention that the stellar temperatures of Abell 30 ($T_{\text{eff}} = 130 \text{ kK}$) and NGC 6153 ($T_{\text{eff}} = 90 \text{ kK}$) are higher than that of PB 8 ($T_{\text{eff}} = 52 \text{ kK}$), so the central star of PB 8 is likely in an early stage of its stellar evolution towards a white dwarf in comparison with Abell 30 and NGC 6153. Accordingly, the planetary nebula PB 8 could be younger and less evolved than the PNe Abell 30 and NGC 6153. More recently, it has been found that PNe with ADFs larger than 10 mostly contain close-binary central stars (Corradi et al., 2015; Jones et al., 2016; Wesson et al., 2017). Currently, there is no evidence for a close-binary central star in PB 8.

Our analysis showed that the bi-abundance hypothesis, which was previously tested in a few PNe with very large abundance discrepancies, could also be used to explain moderate discrepancies between ORL and CEL abundances in most of typical PNe (ADFs ~ 1.6 – 3.2 ; Liu, 2006). It is unclear whether there is any link between the supposed metal-rich inclusions within the nebula and hydrogen-deficient stars. It has been suggested that a (very-) late thermal pulse is responsible for the formation of H-deficient central stars of planetary nebulae (see e.g. Blöcker, 2001; Herwig, 2001; Werner, 2001; Werner & Herwig, 2006). Thermal pulses normally occur during the AGB phase, when the helium-burning shell becomes thermally unstable. The (very-) late thermal pulse occurs when the star moves from the AGB phase towards the white dwarf. It returns the star to the AGB phase and makes a H-deficient stellar surface, so called *born-again* scenario. However, the metal-rich component with $\text{C/O} < 1$ predicted by our photoionization models is in disagreement with the products of a born-again event (Herwig, 2001; Althaus et al., 2005; Werner & Herwig, 2006).

It is also possible that the metal-rich inclusions were introduced by other mechanism such as the evaporation and destruction of planets by stars (Liu, 2003). Recently, Nicholls et al. (2012, 2013) proposed that a non-Maxwellian distribution of electron energies could explain the abundance discrepancy. However, Zhang et al. (2014) found that both the scenarios, bi-abundance models and non-Maxwellian distributed electrons, are adequately consistent with observations of four PNe with very large ADFs. It is unclear whether chemically inhomogeneous plasmas introduce non-Maxwell-Boltzmann equilibrium electrons to the nebula. Alter-

natively, the binarity characteristics such as the orbital separation and companion masses may have a leading role in forming different abundance discrepancies in those PNe with binary central stars (see e.g. Herwig, 2001; Althaus et al., 2005). Further studies are necessary to trace the origin of possible metal-rich knots within the nebula and the cause of various abundance discrepancies in planetary nebulae.

6 ACKNOWLEDGEMENTS

AD is supported by a Macquarie University Research Excellence Scholarship (MQRES) and a Sigma Xi Grants-in-Aid of Research (GIAR). AD thanks the anonymous referee for helpful suggestion and comments that improved the paper, Helge Todt for providing the PoWR models for expanding atmospheres and valuable comments, Jorge García-Rojas and Miriam Peña for providing the Magellan Telescope data and helpful comments, Ralf Jacob for sharing results from radiation-hydrodynamics simulations and valuable suggestions, Christophe Morisset for illuminating discussions and corrections, Quentin A. Parker for providing the 2010 ANU 2.3-m data, David J. Frew for helping with the ANU observing proposal, Kyle DePew for carrying out the 2010 ANU observing run, and Roger Wesson for sharing the program EQUIB (originally written by I. D. Howarth and S. Adams at UCL). The computations in this paper were run on the NCI National Facility in Canberra, Australia, which is supported by the Australian Commonwealth Government, the swinSTAR supercomputer at Swinburne University of Technology, and the Odyssey cluster supported by the FAS Division of Science, Research Computing Group at Harvard University.

REFERENCES

- Acker A., Neiner C., 2003, *A&A*, **403**, 659
- Althaus L. G., Serenelli A. M., Panei J. A., Córscico A. H., García-Berro E., Scóccola C. G., 2005, *A&A*, **435**, 631
- Bautista M. A., 1999, *ApJ*, **527**, 474
- Blöcker T., 2001, *Ap&SS*, **275**, 1
- Corradi R. L. M., García-Rojas J., Jones D., Rodríguez-Gil P., 2015, *ApJ*, **803**, 99
- Danehkar A., 2015, *ApJ*, **815**, 35
- Danehkar A., Parker Q. A., 2015, *MNRAS*, **449**, L56
- Danehkar A., Parker Q. A., Ercolano B., 2013, *MNRAS*, **434**, 1513
- Danehkar A., Todt H., Ercolano B., Kniazev A. Y., 2014, *MNRAS*, **439**, 3605
- Danehkar A., Parker Q. A., Steffen W., 2016, *AJ*, **151**, 38
- Delgado-Inglada G., Morisset C., Stasińska G., 2014, *MNRAS*, **440**, 536
- Dopita M., Hart J., McGregor P., Oates P., Bloxham G., Jones D., 2007, *Ap&SS*, **310**, 255
- Dopita M., et al., 2010, *Ap&SS*, **327**, 245
- Egan M. P., et al., 2003, VizieR Online Data Catalog: V/114, 5114
- Ercolano B., Storey P. J., 2006, *MNRAS*, **372**, 1875
- Ercolano B., Barlow M. J., Storey P. J., Liu X.-W., 2003a, *MNRAS*, **340**, 1136
- Ercolano B., Morisset C., Barlow M. J., Storey P. J., Liu X.-W., 2003b, *MNRAS*, **340**, 1153
- Ercolano B., Barlow M. J., Storey P. J., Liu X.-W., Rauch T., Werner K., 2003c, *MNRAS*, **344**, 1145
- Ercolano B., Wesson R., Zhang Y., Barlow M. J., De Marco O., Rauch T., Liu X.-W., 2004, *MNRAS*, **354**, 558
- Ercolano B., Barlow M. J., Storey P. J., 2005, *MNRAS*, **362**, 1038
- Frew D. J., Bojičić I. S., Parker Q. A., 2013, *MNRAS*, **431**, 2
- Galavis M. E., Mendoza C., Zeppen C. J., 1995, *A&AS*, **111**, 347
- García-Lario P., Manchado A., Ulla A., Manteiga M., 1999, *ApJ*, **513**, 941
- García-Rojas J., Peña M., Peimbert A., 2009, *A&A*, **496**, 139
- Gesicki K., Zijlstra A. A., Acker A., Górny S. K., Goździewski K., Walsh J. R., 2006, *A&A*, **451**, 925
- Gonçalves D. R., Ercolano B., Carnero A., Mampaso A., Corradi R. L. M., 2006, *MNRAS*, **365**, 1039
- Gorny S. K., Stasińska G., Tyłenda R., 1997, *A&A*, **318**, 256
- Gräfener G., Koesterke L., Hamann W.-R., 2002, *A&A*, **387**, 244
- Grieve M. F. R., Ramsbottom C. A., Hudson C. E., Keenan F. P., 2014, *ApJ*, **780**, 110
- Hamann W.-R., Gräfener G., 2004, *A&A*, **427**, 697
- Hanner M. S., 1988, in *Infrared Observations of Comets Halley and Wilson and Properties of the Grains*. pp 22–49
- Helou G., Walker D. W., 1988, *Infrared astronomical satellite (IRAS) catalogs and atlases*, **7**, 1
- Henry R. B. C., Speck A., Karakas A. I., Ferland G. J., Maguire M., 2012, *ApJ*, **749**, 61
- Herwig F., 2001, *Ap&SS*, **275**, 15
- Howarth I. D., Adams S., 1981, Program EQUIB, University College London
- Howarth I. D., Adams S., Clegg R. E. S., Ruffe D. P., Liu X.-W., Pritchett C. J., Ercolano B., 2016, EQUIB: Atomic level populations and line emissivities calculator, Astrophysics Source Code Library, ascl:1603.005
- Hudson C. E., Ramsbottom C. A., Scott M. P., 2012, *ApJ*, **750**, 65
- Jaeger C., Mutschke H., Begemann B., Dorschner J., Henning T., 1994, *A&A*, **292**, 641
- Jones D., Wesson R., García-Rojas J., Corradi R. L. M., Boffin H. M. J., 2016, *MNRAS*, **455**, 3263
- Karakas A. I., Lattanzio J. C., 2003, *Publ. Astron. Soc. Australia*, **20**, 393
- Karakas A. I., van Raai M. A., Lugaro M., Sterling N. C., Dinerestein H. L., 2009, *ApJ*, **690**, 1130
- Kingsburgh R. L., Barlow M. J., 1994, *MNRAS*, **271**, 257
- Kisielius R., Storey P. J., Davey A. R., Neale L. T., 1998, *A&AS*, **133**, 257
- Landi E., Del Zanna G., Young P. R., Dere K. P., Mason H. E., 2012, *ApJ*, **744**, 99
- Lebouteiller V., Barry D. J., Spoon H. W. W., Bernard-Salas J., Sloan G. C., Houck J. R., Weedman D. W., 2011, *ApJS*, **196**, 8
- Lebouteiller V., Barry D. J., Goes C., Sloan G. C., Spoon H. W. W., Weedman D. W., Bernard-Salas J., Houck J. R., 2015, *ApJS*, **218**, 21
- Lenzuni P., Natta A., Panagia N., 1989, *ApJ*, **345**, 306
- Liu X.-W., 2003, in Kwok S., Dopita M., Sutherland R., eds, *IAU Symposium Vol. 209, Planetary Nebulae: Their Evolution and Role in the Universe*. p. 339
- Liu X.-W., 2006, in Barlow M. J., Méndez R. H., eds, *IAU Symposium Vol. 234, Planetary Nebulae in our Galaxy and Beyond*. pp 219–226 ([arXiv:astro-ph/0605082](https://arxiv.org/abs/astro-ph/0605082)), doi:10.1017/S1743921306003000
- Liu X.-W., Storey P. J., Barlow M. J., Danziger I. J., Cohen M., Bryce M., 2000, *MNRAS*, **312**, 585
- Liu X.-W., Luo S.-G., Barlow M. J., Danziger I. J., Storey P. J., 2001, *MNRAS*, **327**, 141
- Liu Y., Liu X.-W., Barlow M. J., Luo S.-G., 2004, *MNRAS*, **353**, 1251

- Liu X.-W., Barlow M. J., Zhang Y., Bastin R. J., Storey P. J., 2006, *MNRAS*, **368**, 1959
- Mathis J. S., Rimpl W., Nordsieck K. H., 1977, *ApJ*, **217**, 425
- Miller Bertolami M. M., Althaus L. G., 2007, *MNRAS*, **380**, 763
- Miller Bertolami M. M., Althaus L. G., Olano C., Jiménez N., 2011, *MNRAS*, **415**, 1396
- Molster F. J., Waters L. B. F. M., Tielens A. G. G. M., Barlow M. J., 2002, *A&A*, **382**, 184
- Munoz Burgos J. M., Loch S. D., Ballance C. P., Boivin R. F., 2009, *A&A*, **500**, 1253
- Nicholls D. C., Dopita M. A., Sutherland R. S., 2012, *ApJ*, **752**, 148
- Nicholls D. C., Dopita M. A., Sutherland R. S., Kewley L. J., Palay E., 2013, *ApJS*, **207**, 21
- Parker Q. A., Phillipps S., Pierce M., et al. 2005, *MNRAS*, **362**, 689
- Parthasarathy M., Acker A., Stenholm B., 1998, *A&A*, **329**, L9
- Perinotto M., Schönberner D., Steffen M., Calonaci C., 2004, *A&A*, **414**, 993
- Phillips J. P., 2004, *MNRAS*, **353**, 589
- Porter R. L., Ferland G. J., Storey P. J., Detisch M. J., 2012, *MNRAS*, **425**, L28
- Porter R. L., Ferland G. J., Storey P. J., Detisch M. J., 2013, *MNRAS*, **433**, L89
- Ramsbottom C. A., Bell K. L., Stafford R. P., 1996, *Atomic Data and Nuclear Data Tables*, **63**, 57
- Rauch T., 2003, *A&A*, **403**, 709
- Rola C., Stasińska G., 1994, *A&A*, **282**, 199
- Schönberner D., Jacob R., Steffen M., Perinotto M., Corradi R. L. M., Acker A., 2005a, *A&A*, **431**, 963
- Schönberner D., Jacob R., Steffen M., 2005b, *A&A*, **441**, 573
- Schwarz H. E., Corradi R. L. M., Melnick J., 1992, *A&AS*, **96**, 23
- Stanghellini L., Corradi R. L. M., Schwarz H. E., 1993, *A&A*, **279**, 521
- Stasińska G., Szczerba R., 1999, *A&A*, **352**, 297
- Tayal S. S., Gupta G. P., 1999, *ApJ*, **526**, 544
- Tayal S. S., Zatsarinny O., 2010, *ApJS*, **188**, 32
- Todt H., Peña M., Hamann W.-R., Gräfener G., 2010, *A&A*, **515**, A83
- Tsamis Y. G., Barlow M. J., Liu X.-W., Storey P. J., Danziger I. J., 2004, *MNRAS*, **353**, 953
- Tsamis Y. G., Walsh J. R., Péquignot D., Barlow M. J., Danziger I. J., Liu X.-W., 2008, *MNRAS*, **386**, 22
- Tylenda R., Acker A., Stenholm B., 1993, *A&AS*, **102**, 595
- Tylenda R., Siódmiak N., Górny S. K., Corradi R. L. M., Schwarz H. E., 2003, *A&A*, **405**, 627
- Verner D. A., Yakovlev D. G., 1995, *A&AS*, **109**, 125
- Verner D. A., Yakovlev D. G., Band I. M., Trzhaskovskaya M. B., 1993, *Atomic Data and Nuclear Data Tables*, **55**, 233
- Viegas S. M., Clegg R. E. S., 1994, *MNRAS*, **271**, 993
- Wang W., Liu X.-W., 2007, *MNRAS*, **381**, 669
- Werner K., 2001, *Ap&SS*, **275**, 27
- Werner K., Herwig F., 2006, *PASP*, **118**, 183
- Wesson R., Liu X.-W., Barlow M. J., 2003, *MNRAS*, **340**, 253
- Wesson R., Jones D., García-Rojas J., Corradi R. L. M., Boffin H. M. J., 2017, in Liu X., Stanghellini L., Karakas A., eds, *IAU Symposium Vol. 323, Planetary Nebulae: Multi-Wavelength Probes of Stellar and Galactic Evolution*. pp 70–73 ([arXiv:1612.02215](https://arxiv.org/abs/1612.02215)), doi:10.1017/S1743921317001958
- Yamamura I., Makiuti S., Ikeda N., Fukuda Y., Oyabu S., Koga T., White G. J., 2010, *VizieR Online Data Catalog*, **II**, 2298
- Yuan H.-B., Liu X.-W., Péquignot D., Rubin R. H., Ercolano B., Zhang Y., 2011, *MNRAS*, **411**, 1035
- Zhang Y., Liu X.-W., Zhang B., 2014, *ApJ*, **780**, 93